Optics and Lasers in Engineering 186 (2025) 108781

Contents lists available at ScienceDirect

Optics and Lasers in Engineering

journal homepage: www.elsevier.com/locate/optlaseng

Fast and long-range 3D shape measurement using reference-phase-based number-theoretical temporal phase unwrapping with a MEMS projector

Wei Yin [a,b,c,1], Long Yin [a,b,c,1], Xu Yang [a,b,c], Shijie Feng [a,b,c], Xiaolei Zhang [b], Huai Wang [d], Qian Chen [c], Chao Zuo [a,b,c,*]

[a] Smart Computational Imaging Laboratory (SCILab), School of Electronic and Optical Engineering, Nanjing University of Science and Technology, Nanjing, Jiangsu Province 210094, China
[b] Smart Computational Imaging Research Institute (SCIRI) of Nanjing University of Science and Technology, Nanjing, Jiangsu Province 210019, China
[c] Jiangsu Key Laboratory of Spectral Imaging & Intelligent Sense, Nanjing, Jiangsu Province 210094, China
[d] Suzhou Abham Intelligent Technology Co., Ltd., Suzhou, Jiangsu Province 215000, China

ARTICLE INFO

Keywords:
Fringe projection profilometry
3D imaging
Phase unwrapping
Depth constraint

ABSTRACT

For 3D imaging using fringe projection profilometry (FPP), temporal phase unwrapping (TPU) able to robust absolute phase recovery is essential for accurately measuring complex scenes with surface discontinuities. In the presence of systematic errors and other random noises, the most efficient dual-frequency TPU method generally restricts the frequency of high-frequency phases to about 16, compromising the 3D measurement accuracy. Employing the reference phases based on depth constraint allows for unwrapping the phase map with a higher frequency, albeit at the cost of a narrower measured depth range. In this paper, we present a fast and long-range 3D shape measurement method using reference-phase-based number-theoretical temporal phase unwrapping with a MEMS Projector. By introducing the reference phases into traditional number-theoretical TPU, the proposed method with the aid of the optimal bi-frequency scheme has the ability to efficiently and accurately remove the phase ambiguities of high-frequency fringes, while theoretically circumventing the limitations of the measurement range. Furthermore, simulations and experiments have been carried out to evaluate the absolute phase measurement performance of three groups of classical TPU algorithms using the reference phases, including multi-frequency approach, multi-wavelength approach, and number-theoretical approach. Additionally, the feasibility of our method is validated in two developed 3D imaging sensors using MEMS-based miniaturized projectors for various application scenarios. Owing to the more complex calibration processes and lower projection quality of MEMS projectors in comparison to DLP projectors, experimental results demonstrate that the proposed method is highly available for 3D imaging systems with MEMS projectors, which enhances the efficiency and accuracy of absolute phase measurement, achieving fast, wide-field-of-view, and long-range 3D imaging.

1. Introduction

Optical 3D imaging, as one of the most promising metrology techniques [1,2], enables the quantitative acquisition of three-dimensional (3D) geometric information of objects, and is extensively applied across numerous fields, such as reverse engineering, intelligent manufacturing, and medical plastic surgery. Mainstream optical 3D imaging methods include stereo vision [3–7], time of flight [8–11], laser line scanning [12], and structured light projection [13–16], related instruments have been employed for robot navigation, autonomous driving, and 3D defect detection. With the advances of high-performance cameras and structured light projection techniques, fringe projection profilometry (FPP) has become a classic optical 3D sensing method thanks to its distinguishing characteristics in high precision, full-field measurement, and high resolution. In FPP, the projected fringe patterns are modulated by the object profiles and handled to restore the desired phase distribution associated with the tested surfaces using various fringe pattern analysis methods [17–23]. The spatial phase-demodulation (SPD) method,

* Corresponding author.
E-mail address: zuochao@njust.edu.cn (C. Zuo).
[1] They contributed equally to this work.

https://doi.org/10.1016/j.optlaseng.2024.108781
Received 6 November 2024; Received in revised form 6 December 2024; Accepted 12 December 2024

Available online 18 December 2024

as the most efficient fringe analysis technique, has access to the phase retrieval of a single-frame fringe. However, such methods usually yield low-quality coarse phases due to the spectrum overlapping, which limits their measurement precision for dynamic 3D acquisition. Different from SPD methods, phase-shifting (PS) approaches achieve pixel-wise and high-accuracy phase measurements unaffected by ambient lighting, but requires at least three fringe patterns theoretically. In addition, both methods perform the arctangent function for phase recovery, bringing the obtained wrapped phases with 2π phase jumps. Consequently, phase unwrapping is a key procedure in FPP to remove the ambiguities of the wrapped phases and actualize absolute 3D measurement.

These existing phase unwrapping approaches can be divided into three basic classifications: spatial phase unwrapping [24–27], temporal phase unwrapping (TPU) [28–33], and stereo phase unwrapping [34–41], where additional patterns or more constraints need to be utilized for phase unwrapping to achieve absolute 3D measurement. The fundamental assumption made by spatial phase unwrapping is that the phase maps to be unwrapped have a global continuity. Consequently, this assumption does not hold at disjunct profiles or abrupt depth with phase changes greater than 2π, causing final measurement results with continuity artifacts and depth ambiguities.

To overcome this challenge, TPU methods are exploited to realize pixel-by-pixel absolute phase recovery through the temporal study of multiple sets of wrapped phases with different frequencies. Three representational algorithms fall into TPU: multi-frequency approach [42,43], multi-wavelength approach [44,45], and number-theoretical approach [46–48]. In multi-frequency approach, since the single-frequency wrapped phase is also a continuous and absolute phase, it can be utilized to directly unwrap high-frequency phases according to the relation between their frequencies. In the presence of systematic errors and other random noises during experiments, its high-frequency phase unwrapping capability is severely restricted, resulting in limited 3D measurement accuracy. Therefore, it generally requires an extra group of fringe patterns with intermediate frequencies to unwrap the phase map with the higher frequency, albeit at the cost of an extended projected pattern sequence. Similarly, multi-wavelength approach handles two sets of wrapped phases with close wavelengths to synthesize a beat-frequency phase with a larger wavelength (the frequency is less than 1). It can be found that multi-wavelength approach generates a fundamental absolute phase in another way for high-frequency phase unwrapping. Different from the two methods above, number-theoretical approach adopts two sets of wrapped phases with a mutually prime relationship between wavelengths to encode the periodic order of the phases, realizing efficient absolute phase unwrapping through a lookup table. The least common multiple of the wavelengths of two sets of fringe patterns determines the unambiguous range of absolute phase unwrapping. Therefore, how to determine the bi-frequency fringe scheme to achieve high-frequency phase unwrapping in a global range is an issue of concern. Furthermore, the success rate and noise resistance of three TPU methods are analyzed according to a schematic statistical noise model that the multi-frequency method has excellent phase unwrapping performance, but the multi-wavelength method is severely affected by noise [29].

In addition, by pre-setting the measurement range of FPP systems, depth constraint can be utilized to eliminate the phase ambiguities located outside the 3D measurement volume, enhancing the performance of phase unwrapping. Following this idea, An et al. [49] manually created an absolute phase Φ_{min} located at a suppositional depth plane as the reference phase to actualize pixel-wise phase unwrapping of high-frequency phases within a strict depth range (approximately 58 mm). Afterward, Hyun et al. [50,51] exploited the minimum phase constraint to multi-frequency approach and step-coding method to elevate the frequency of low-frequency phases [50] or the step signal [51], thereby improving the measurement accuracy using the phases with higher frequency. However, to maintain the phase unwrapping reliability, the period of high-frequency phases is generally restricted to about 30 pixels. Duan et al. [52] reported an adaptive phase unwrapping technique within an unlimited depth range to achieve absolute phase unwrapping of isolated objects through some edge detection and object detection algorithms. But, it may not be applicable to complex scenes, such as two objects that are separated in depth but occlude each other on the imaging plane.

On the other hand, for stereo phase unwrapping, an additional auxiliary camera is introduced to directly recover high-frequency absolute phases by utilizing the geometric constraint in stereo vision [34,36,40,53,54]. Weise et al. [34] introduced the geometric constraint into a dual-camera FPP system, which achieved dynamic 3D reconstruction of the human body using 3-step phase-shifting fringe patterns. Li et al. [36] exploited the trifocal tensor constraint to independently determine for homologous points with similar phases of each valid pixel, achieving dynamic 3D measurement of complex scenes. While ensuring the stability of stereo phase unwrapping, the period of high-frequency fringes is generally around 20, compromising the 3D measurement accuracy. It is easy to understand that introducing multi-view geometric constraints using more cameras removes the ambiguities of high-frequency phases thoroughly. Following this idea, Peng et al. [53] utilized multiple phase consistency checks between three cameras to fulfill high-accuracy 3D imaging. Tao et al. [40] built a quad-camera FPP system based on position optimization, and a weighted phase difference scheme between multiple perspectives is present to acquire high-frequency absolute phases with 48 periods.

Additionally, the prerequisite for stereo phase unwrapping is the projector calibration. The mainstream projector calibration methods [55,56] regard the projector as an inverse camera and establish the image transformation between the camera and the projector with the aid of a series of horizontal and vertical fringe patterns, which is highly suitable for FFP systems based on digital light processing (DLP) projectors. As the core component of FPP systems, DLP projectors are commonly used to project high-quality fringe patterns for high-accuracy 3D measurement, but their characteristics of high cost and low optical power bring unparalleled challenges to portable and long-range 3D imaging. Different from DLP projectors, electrostatically driven MEMS projectors, which have the advantages of miniaturization and high intensity, operate MEMS galvanometers with a high-frequency resonant motion to reflect the incident 1D line laser, enabling high-speed 1D scanning projection of uni-directional fringe patterns. However, MEMS-based FPP systems often suffer from the low accuracy and complex process of existing projector calibration methods based on the phase-height model [57,58]. In addition, the initial phase of the MEMS scanning mirror may change over time due to temperature drift, which severely reduces the projector calibration accuracy and deteriorates the 3D reconstruction quality [59]. In this paper, we introduced the reference phases into traditional number-theoretical TPU to achieve fast and long-range 3D shape measurement based on a MEMS projector. With the aid of the optimal bi-frequency fringe scheme, the proposed method enables more accurate and efficient absolute phase unwrapping of the high-frequency fringes with 64 periods within a larger depth range without the projector calibration. Further, the performance of three groups of classical TPU algorithms using the reference phases is analyzed under both simulation and experimental conditions. Experiments proved that the proposed method enhances the phase unwrapping performance in terms of noise resistance and depth range compared with multi-frequency approach and multi-wavelength approach using the reference phases, achieving fast, accurate, and long-distance 3D profile measurement for complex scenes with many isolated objects.

2. Principle

2.1. Bi-frequency (3+2) phase-shifting algorithm

In this subsection, we will briefly introduce the bi-frequency phase-shifting (PS) algorithm to achieve high-frequency and low-frequency

phase retrieval for fast absolute 3D measurement [21]. High-frequency fringe images I_n^H based on conventional three-step PS methods are first captured:

$$I_n^H = A^H + B^H \cos(\Phi^H - 2n\pi/3), \tag{1}$$

where A^H, B^H, and Φ^H are the average intensity, the intensity modulation, and the phase distribution of high-frequency fringes, and n represents the phase-shifting index $n = 0, 1, 2$. For PS methods, the wrapped phase map ϕ^H and two by-products (A^H, B^H) can be obtained:

$$\phi^H = \tan^{-1} \frac{\sum_{n=0}^{2} I_n^H \sin(2n\pi/3)}{\sum_{n=0}^{2} I_n^H \cos(2n\pi/3)}, \tag{2}$$

$$A^H = \frac{1}{3} \sum_{n=0}^{2} I_n^H, \tag{3}$$

$$B^H = \frac{1}{2} \sqrt{\left[\sum_{n=0}^{2} I_n^H \sin\frac{2n\pi}{3}\right]^2 + \left[\sum_{n=0}^{2} I_n^H \cos\frac{2n\pi}{3}\right]^2}. \tag{4}$$

For the bi-frequency PS algorithm, suppose the average intensity of the collected fringes remains constant during a single 3D measurement, low-frequency fringe images have the same A^H as the high-frequency ones:

$$I_1^L = A^H + B^L \sin(\Phi^L), \tag{5}$$

$$I_2^L = A^H + B^L \cos(\Phi^L). \tag{6}$$

Then, the low-frequency wrapped phase map ϕ^L can be calculated:

$$\phi^L = \tan^{-1} \frac{I_1^L - A^H}{I_2^L - A^H}. \tag{7}$$

In the bi-frequency PS algorithm, two wrapped phases with different frequencies are demodulated using only five fringe patterns and further unwrapped using different temporal phase unwrapping methods.

2.2. Number-theoretical temporal phase unwrapping using the reference phases

Since PS algorithms adopt the arctangent function for phase measurement in Eqs. (2) and (7), the extracted phases have a 2 π phase jump:

$$\Phi^H = \phi^H + 2\pi k^H, \tag{8}$$

$$\Phi^L = \phi^L + 2\pi k^L, \tag{9}$$

and the relationship is linked inherently:

$$\Phi^H = \frac{\lambda^L}{\lambda^H} \Phi^L, \tag{10}$$

where Φ^H and Φ^L are the high-frequency and low-frequency absolute phases, k^H, k^L, λ^H, and λ^L are the corresponding fringe orders and wavelengths. Based on the principle of number-theoretical temporal phase unwrapping [30,48,60], according to Eqs. (8)-(10), k^H and k^L can be calculated by the following formula:

$$\frac{\lambda^L \phi^L - \lambda^H \phi^H}{2\pi} = \lambda^H k^H - \lambda^L k^L. \tag{11}$$

Since two phases ϕ^H and ϕ^L both change periodically ranging from 0 to 2π on different wavelengths, the value of $\lambda^L \phi^L - \lambda^H \phi^H$ is unique within the scope $LCM(\lambda^H, \lambda^L)$. $LCM(\lambda^H, \lambda^L)$ outputs the least common multiple for its input parameters. In addition, due to the integer type of k^H and k^L, Eq. (11) can be rewritten as:

$$Round(\frac{\lambda^L \phi^L - \lambda^H \phi^H}{2\pi}) = \lambda^H k^H - \lambda^L k^L, \tag{12}$$

where a unique combination (k^H, k^L) can be directly looked up according to $Round(\frac{\lambda^L \phi^L - \lambda^H \phi^H}{2\pi})$, thereby achieving absolute phase unwrapping within the scope $LCM(\lambda^H, \lambda^L)$. And k^i ranges from 0 to $p^i - 1 (i = L, H)$:

$$Round(\frac{p^H \phi^L - p^L \phi^H}{2\pi}) = p^L k^H - p^H k^L, \tag{13}$$

$$p^H = LCM(\lambda^H, \lambda^L)/\lambda^H, \tag{14}$$

$$p^L = LCM(\lambda^H, \lambda^L)/\lambda^L, \tag{15}$$

where p^H and p^L stand for the period number of fringes with the corresponding wavelengths in the unambiguous scope $LCM(\lambda^H, \lambda^L)$. In traditional number-theoretical TPU, the bi-frequency fringe scheme needs to be meticulously determined to satisfy $LCM(\lambda^H, \lambda^L) \geq W$ for unwrapping the high-frequency phase globally, where W is the horizontal resolution of projected patterns. However, this limitation leads to an increase in the wavelengths of bi-frequency fringes, reducing its 3D accuracy.

To solve the issue above, the reference phases based on depth constraint are brought in number-theoretical TPU to achieve more accurate and efficient absolute phase unwrapping with higher frequency. In the proposed method, the built FPP-based 3D imaging system is first moved along the Z-axis to collect absolute phases of the reference plane at the specific depth Z_{ref}, such as the nearest and farthest boundaries of the whole measurement volume as shown in Fig. 1. Suppose the measurement range of our FPP system is $[Z_{min}, Z_{max}]$, due to the linear dependence between the absolute phase Φ_{ref}^H and the measured Z_{ref} [30,40], the range of Φ_{ref}^H can be defined as:

$$\Phi_{min}^H \leq \Phi_{ref}^H \leq \Phi_{max}^H, \tag{16}$$

where Φ_{max}^H and Φ_{min}^H are the reference phases obtained using a series of multi-step phase-shifting fringe images and multi-frequency TPU approach. According to Eqs. (8) and (16), the range of k^H can be further determined:

$$Ceil(\frac{\Phi_{min}^H - \phi^H}{2\pi}) \leq k^H \leq Floor(\frac{\Phi_{max}^H - \phi^H}{2\pi}). \tag{17}$$

It can be found that the range of k^H is narrowed from $[0, p^i - 1]$ to $[Ceil(\frac{\Phi_{min}^H - \phi^H}{2\pi}), Floor(\frac{\Phi_{max}^H - \phi^H}{2\pi})]$ using the reference phases based on depth constraint, which means that the phase ambiguities to be eliminated are significantly reduced based on Eq. (17). Therefore, for number-theoretical TPU using the reference phases, the requirement of the unambiguous scope $LCM(\lambda^H, \lambda^L)$ can be adjusted from the global range to the local range:

$$LCM(\lambda^H, \lambda^L) \geq (k_{max}^H - k_{min}^H)\lambda^H. \tag{18}$$

The proposed method can elevate the frequencies of dual-frequency fringes and realize high-frequency phase unwrapping, enabling high-precision 3D reconstruction.

2.3. Simulation for three groups of classical TPU algorithms using the reference phases

For FPP, typical temporal phase unwrapping (TPU) methods include multi-frequency approach (MF-TPU) [42,43], multi-wavelength approach (MW-TPU) [44,45], and number-theoretical approach (NT-TPU) [46–48]. The unwrapping performance of these TPU algorithms has been analyzed and discussed under the same noise conditions that MF-TPU can provide the highest unwrapping reliability and the best noise robustness [29]. However, for these three groups of TPU algorithms using the reference phases, the final conclusions they arrived at may be completely different. Here, the performance of TPU methods will be compared by calculating the correctness of the recovered

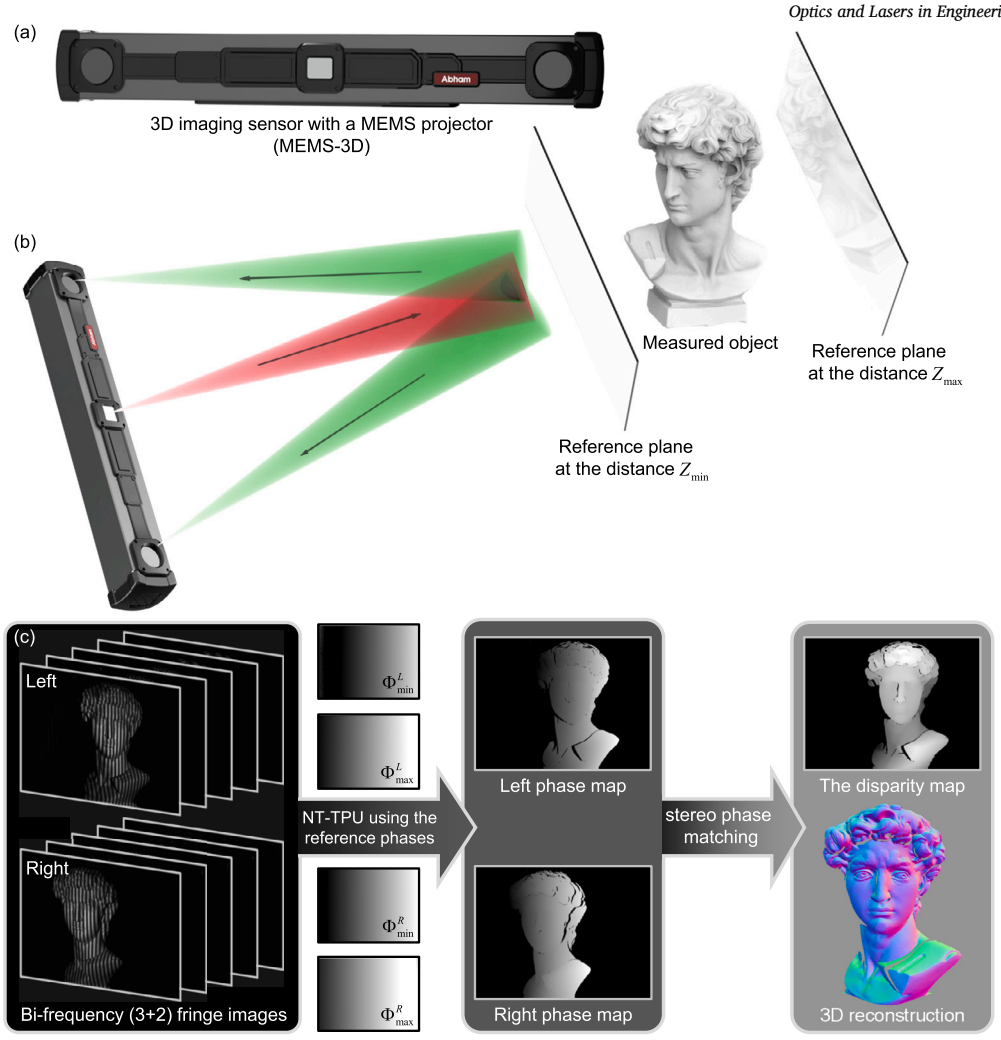

Fig. 1. Overview of 3D shape measurement using reference-phase-based NT-TPU with a MEMS projector. (a) Photograph of the developed 3D imaging sensor (MEMS-3D) with a MEMS projector. (b) The diagram of the proposed NT-TPU using the reference phases. (c) The flowchart of 3D reconstruction using the proposed method.

high-frequency fringe orders. Similar to Eq. (13), all three TPU methods calculate the orders of high-frequency phases through the general weighted difference of the bi-frequency phases:

$$k^H \Leftarrow Round(\frac{\alpha\phi^L - \beta\phi^H}{2\pi}), \tag{19}$$

where α and β are varied with different TPU methods:

$$\begin{cases} \alpha = \lambda^L/\lambda^H, \ \beta = 1; & \text{for MF-TPU} \\ \alpha = -\frac{\lambda^L}{\lambda^L-\lambda^H}, \ \beta = -\frac{\lambda^H}{\lambda^L-\lambda^H}; & \text{for MW-TPU} \\ \alpha = \frac{LCM(\lambda^H,\lambda^L)}{\lambda^H}, \ \beta = \frac{LCM(\lambda^H,\lambda^L)}{\lambda^L}; & \text{for NT-TPU} \end{cases} \tag{20}$$

Once the reference phases based on depth constraint are introduced into MF-TPU, the low-frequency ones in the bi-frequency fringe scheme will no longer be 1, and its periodic order is limited to the range:

$$k^L_{min} \le k^L \le k^L_{max}. \tag{21}$$

To enable the unambiguous low-frequency phase unwrapping theoretically, the reference phases need to meet the following requirements:

$$k^L = k^L_{min} = k^L_{max}. \tag{22}$$

$$\Phi^L_{max} - \Phi^L_{min} < 2\pi. \tag{23}$$

Based on Eqs. (22) and (23), the low-frequency phase ϕ^L can be successfully unwrapped with the aid of the reference phases based on an eligible depth range. While ensuring the stability of phase unwrapping and an acceptable measurement range, the frequency of ϕ^L is generally limited to about 8.

On the other hand, for MW-TPU using the reference phases, a beat-frequency phase is first synthesized by calculating the difference between bi-frequency phases:

$$\phi^{beat} = \phi^H - \phi^L, \tag{24}$$

$$\lambda^{beat} = \frac{\lambda^L\lambda^H}{\lambda^L - \lambda^H}, \tag{25}$$

The synthetic phase ϕ^{beat} is widely regarded as an unambiguous phase to unwrap high-frequency phases. Like MF-TPU, the reference phases are used to unwrap the synthetic phase ϕ^{beat} with higher frequency, which in turn enables absolute measurement of the high-frequency phase. Therefore, the reference phases in MW-TPU have similar constraints as that in MF-TPU.

Different from the two TPU methods above, two sets of wrapped phases with relatively prime wavelengths are utilized to encode their periodic orders in NT-TPU. The reference phases limit the periodic order of high-frequency phases to the following range:

$$k^H_{min} \le k^H \le k^H_{max}. \tag{26}$$

How to search the optimal scheme of the bi-frequency fringes is our main concern for enhancing the performance of NT-TPU using the reference

Table 1
Bi-frequency schemes based on different TPU methods using the reference phases.

Parameters	MF-TPU	MW-TPU	NT-TPU
λ^H	19 pixels	19 pixels	19 pixels
λ^L	228 pixels	22 pixels	63 pixels
L_{range}	228 pixels	139.33 pixels	190 pixels
$\Delta\phi$	19 $\pi/247$ rad	3 $\pi/41$ rad	$3\pi/41$ rad

phases. According to Eq. (13), the overall phase error $\Delta\phi$ of NT-TPU can be obtained:

$$\frac{p^H\Delta\phi^L - p^L\Delta\phi^H}{2\pi} = \Delta\phi\frac{p^H + p^L}{2\pi}, \tag{27}$$

where $\Delta\phi^L$ and $\Delta\phi^H$ represent the phase errors of ϕ^L and ϕ^H, and $\Delta\phi$ is the maximum between $\Delta\phi^L$ and $\Delta\phi^H$. And then, the range of $\Delta\phi$ can be derived to avoid phase unwrapping errors [30]:

$$\Delta\phi\frac{p^H + p^L}{2\pi} < 0.5G_{min}, \tag{28}$$

$$\Delta\phi < \frac{\pi}{p^H + p^L}G_{min}, \tag{29}$$

where G_{min} is the minimum gap of $p^Lk^H - p^Hk^L$ within the predefined depth range based on Eq. (26). Subsequently, there is only one thing to maximize $\frac{\pi}{p^H+p^L}G_{min}$ by traversing all possible bi-frequency schemes.

To verify the performance of all three TPU methods using the reference phases, we conducted a simulation experiment for absolute phase measurement of a planar target under different depth constraints. Experimental parameters of bi-frequency schemes based on different TPU methods using the reference phases are shown in Table 1. In this simulation, W is 1216 pixels, which represents the horizontal resolution of projected patterns. The frequencies of the high-frequency phases in these three TPU methods are uniformly set to 64, and their wavelengths are 19 pixels. The depth constraint L_{range} is the pixel range in the projection plane converted from the depth range in the 3D imaging space. Since the range of the reference phases cannot exceed 2π in MF-TPU according to Eq. (23), the range of $\Delta\phi$ can be derived to avoid phase unwrapping errors, i.e., $\frac{\lambda^H}{\lambda^L+\lambda^H}\pi$. To realize absolute phase unwrapping within a larger depth range, the wavelength of the low-frequency phase is set to 228 pixels as same as L_{range}, and the corresponding phase noise tolerance $\Delta\phi$ is 19 $\pi/247$ rad. In the same way, L_{range} is set to the wavelength of the synthetic phase ϕ^{beat} in MW-TPU, and the phase noise tolerance is inferred to $\frac{\lambda^L-\lambda^H}{\lambda^L+\lambda^H}\pi$. In order to achieve phase unwrapping performance comparable to that of MF-TPU, the low-frequency wavelength of MW-TPU is set to 22 pixels, and $\Delta\phi$ is 3 $\pi/41$ rad. Therefore, the wavelength of the synthetic phase ϕ^{beat} is 139.33 pixels as same as L_{range}.

For NT-TPU using the reference phases, the search strategy of the optimal bi-frequency fringes is utilized to traverse all possible bi-frequency combinations to maximize the noise tolerance of phase unwrapping. Specifically, it is necessary to determine the unambiguous measurement range and the noise tolerance of each bi-frequency fringe combination with different low-frequency wavelengths. Take $\lambda^H = 19$ pixels and $\lambda^L = 63$ pixels as an example, the distribution of $p^Lk^H - p^Hk^L$ is first calculated based on Eq. (13) and plotted as shown in Fig. 2. Fig. 2(a) shows that the theoretical unambiguous range of this combination is 1197 pixels, but once the phase error $\Delta\phi$ is greater than $\frac{\pi}{p^H+p^L}$ causing phase unwrapping errors, which demonstrates high sensitivity of NT-TPU to noise. Further, as shown in the magnified view of Fig. 2(b), the distribution of $p^Lk^H - p^Hk^L$ appears an obvious periodic change with a narrower wavelength. Once the unambiguous range is determined to be 190 pixels, the minimum gap G_{min} is 6 within the local depth scope, and the corresponding noise tolerance of phase unwrapping $\Delta\phi$ will be raised from $\pi/82$ rad to $3\pi/41$ rad.

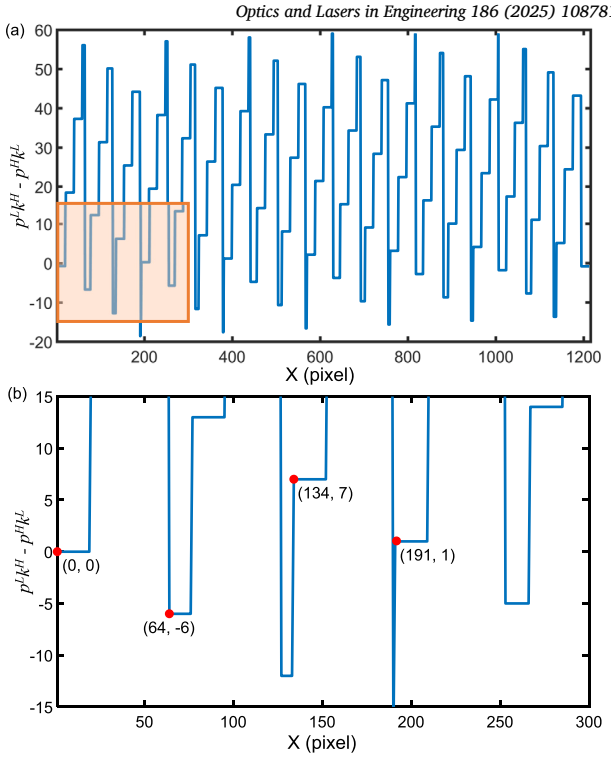

Fig. 2. The specific process of the search strategy of the optimal bi-frequency fringes. (a) The distribution of $p^Lk^H - p^Hk^L$ for $\lambda^H = 19$ pixels and $\lambda^L = 63$ pixels. (b) The magnified view of the distribution.

Secondly, Fig. 3 shows the simulation results of phase unwrapping for three TPU approaches using the reference phases. In order to quantitatively calculate the phase unwrapping accuracy, the error rates are calculated for the absolute phases with noise under different depth constraints compared with the noise-free ground truth. Based on the noise model of phase-shifting profilometry [29], the variance of absolute phase error corresponding to fringe patterns has positive correlation with the noise variance and inversely related to the square of the fringe frequency and the phase-shifting step. Specifically, the phase noises with different variances acted on high-frequency and low-frequency phases in different TPU approaches to analyze the absolute phase reconstruction quality under different noise levels. As shown in Figs. 3(a) and (d), as the noise level increases, the reconstructed phases of MF-TPU in a larger depth range are deteriorated by phase noise, with a substantial increase in the error rates of phase unwrapping from 0.7617% to 5.6097%. It demonstrates that MF-TPU is incapable of achieving global phase unwrapping within a larger depth scope due to its inherent limitations based on Eq. (23). In Figs. 3(b) and (e), it is evident that MW-TPU is able to achieve global and unambiguous phase unwrapping, but at the expense of a narrower measurement range compared with MF-TPU. Different from MF-TPU and MW-TPU, NT-TPU significantly expands the depth constraint to 190 pixels, while achieving global phase unwrapping with a comparable error rate (0.0928% and 0.5317%) as shown in Figs. 3(c) and (f). The simulation results of phase unwrapping confirm that the optimal bi-frequency scheme is crucial to enhance the high-frequency phase unwrapping performance of NT-TPU using the reference phases, enabling efficient, long-range, and high-precision 3D shape measurement.

3. Experiments

To assess the 3D imaging performance of the proposed NT-TPU method using the reference phases, two miniaturized 3D sensors with different geometric parameters have been developed to achieve fast, wide-field-of-view, and high-precision 3D measurements for various ap-

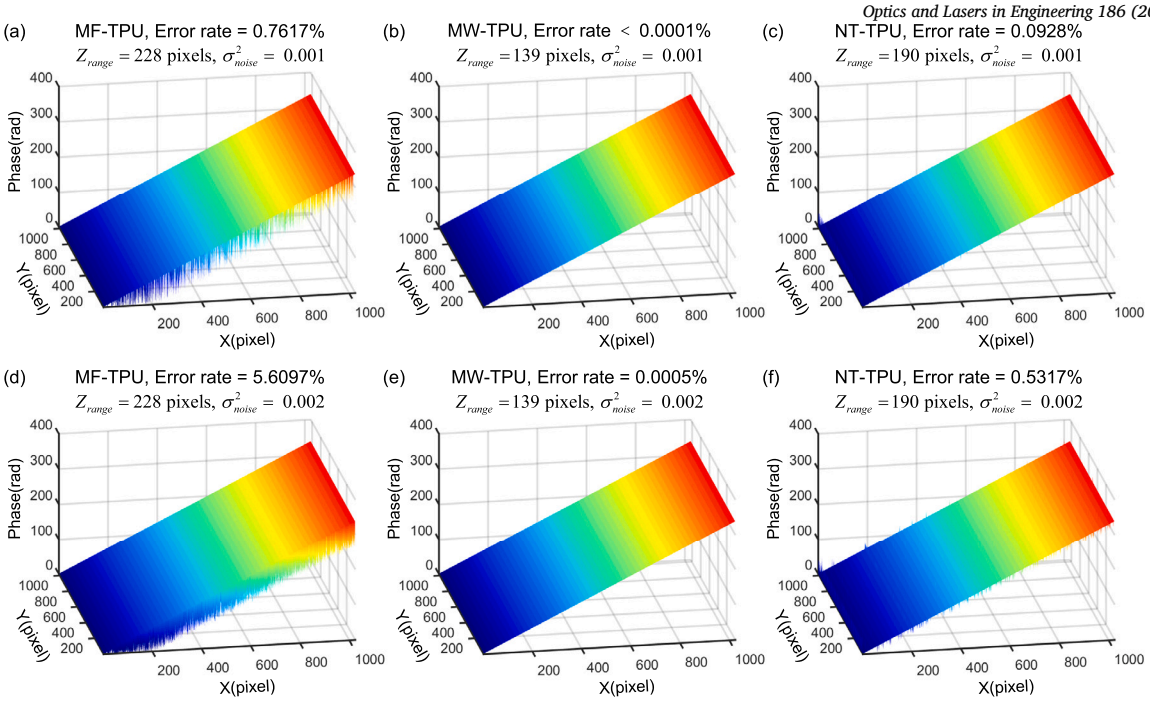

Fig. 3. The simulation results of phase unwrapping for different TPU approaches (λ^H = 19 pixels) using the reference phases. (a) and (d) MF-TPU approach (λ^L = 228 pixels) under different noise levels. (b) and (e) MW-TPU approach (λ^L = 22 pixels) under different noise levels. (c) and (f) NT-TPU approach (λ^L = 63 pixels) under different noise levels.

plication scenarios. Both of these two 3D sensors are mainly composed of two CMOS monochrome cameras and a MEMS-based blue light projector with a resolution of 1×1024 pixels. The electrostatically driven MEMS projector has the advantages of miniaturization and high intensity, which can actualize high-speed 1D scanning projection of bi-frequency (3+2) fringe patterns at a projection rate of up to 1,200 FPS. In addition, two 3D sensors (named MEMS-3D and MEMS-3D-Nano) adopt different combinations of CMOS cameras and lenses to perceive 3D targets located at different distances. For the long-range 3D sensor (MEMS-3D), two CMOS cameras (Sony IMX265) with a resolution of 2048×1536 pixels are equipped with the 12 mm (focal length) lens, and their baseline is approximately 0.4 m to measure objects within a depth range of 1.0 m to 3.0 m, where the predefined disparity range is configured to -250 to 690 pixels. To achieve fast and near-field 3D imaging, for the miniaturized 3D sensor (MEMS-3D-Nano) with a narrow baseline of 0.1 m, two CMOS cameras (Smartsens SC130GS) are executed to collect stereo fringe images with a SXGA resolution (1280×1024 pixels) at 100 Hz. The disparity range of the developed 3D imaging sensor (MEMS-3D-Nano) is configured as -160 pixels to 80 pixels to enable 3D scene measurement ranging from 0.4 m to 1.3 m at 20 FPS.

3.1. Long-range 3D reconstruction of complex targets

First of all, two isolated large-scale objects are measured by our 3D sensor (MEMS-3D) to describe the 3D imaging process of NT-TPU using the reference phases, showcasing its advanced capability of efficient and long-distance 3D measurement. The scene to be measured consists of a Lu Xun plaster located at 1.1 m (the nearest position) and a geometric model at the farthest end of the whole measurement space, and the corresponding fringe images of left camera are revealed in Fig. 4 (a). However, as the measurement distance increases, our 3D sensor is unable to simultaneously capture high-quality fringe patterns of two objects at different distances through only a single exposure. As demonstrated in Figs. 4 (a)-(c) and (e)-(g), a hybrid 3D imaging strategy utilizing the double exposure is employed to accurately retrieve bi-frequency wrapped phases of the Lu Xun and the geometric model, respectively. In our approach, the high-precision and dense absolute phases of the reference planes positioned at 1 m and 3 m are pre-collected by combining N-step PSP and MF-TPU algorithms. According to Eq. (17), the reference phases are introduced into traditional number-theoretical TPU to significantly reduce the search range of its phase period, thus enabling pixel-wise absolute phase unwrapping. When the exposure time of the stereo camera is configured to 10 ms, the absolute phase distribution of the Lu Xun model can be reliably recovered, but the geometry still has non-negligible fringe order errors as shown in the magnified region of Fig. 4 (d). After gradually increasing the exposure time to 50 ms for enhancing the phase quality of the geometric model in Fig. 4 (h), the phase maps with different exposure times can be effectively fused based on the phase modulation, thereby achieving global and unambiguous phase unwrapping as shown in Fig. 4 (i). Once the mixed absolute phases from left and right cameras are obtained, stereo phase matching based on geometric constraints is executed to output the disparity map in Fig. 4 (j). Subsequently, the disparity data is reconstructed to final 3D measurement results with high completeness within a larger depth scope, demonstrating the ability of the proposed method to realize long-distance and high-precision 3D imaging for large-sized complex surfaces.

Next, MF-TPU and MW-TPU approaches using the reference phases are exploited to reconstruct the same target scene for verifying the conclusion of the simulation above. After adjusting the distance between the 3D sensor and the geometric model, Figs. 5 and 6 showed that it is impossible to directly unwrap the low-frequency phase in MF-TPU or the synthetic phase in MW-TPU using the depth constraints when the geometric model is at 2.3 m or 1.9 m. Experimental results show that as the measurement distance increases, MF-TPU is affected by low-frequency phase noises and cannot achieve reliable absolute phase unwrapping, while MW-TPU is limited by its inherent defects for long-distance 3D measurement. According to the experimental parameters of bi-frequency fringe schemes in Table 1, the unambiguous measurement range of NT-TPU is about 1.36 times that of MW-TPU in the projection plane. Since the MEMS projector was not calibrated, the disparity range between the left and right cameras can be used to demonstrate the measurement range. For the developed 3D sensor (MEMS-3D), the 3D measurement range that NT-TPU can achieve is 1 m to 3 m, the corresponding disparity

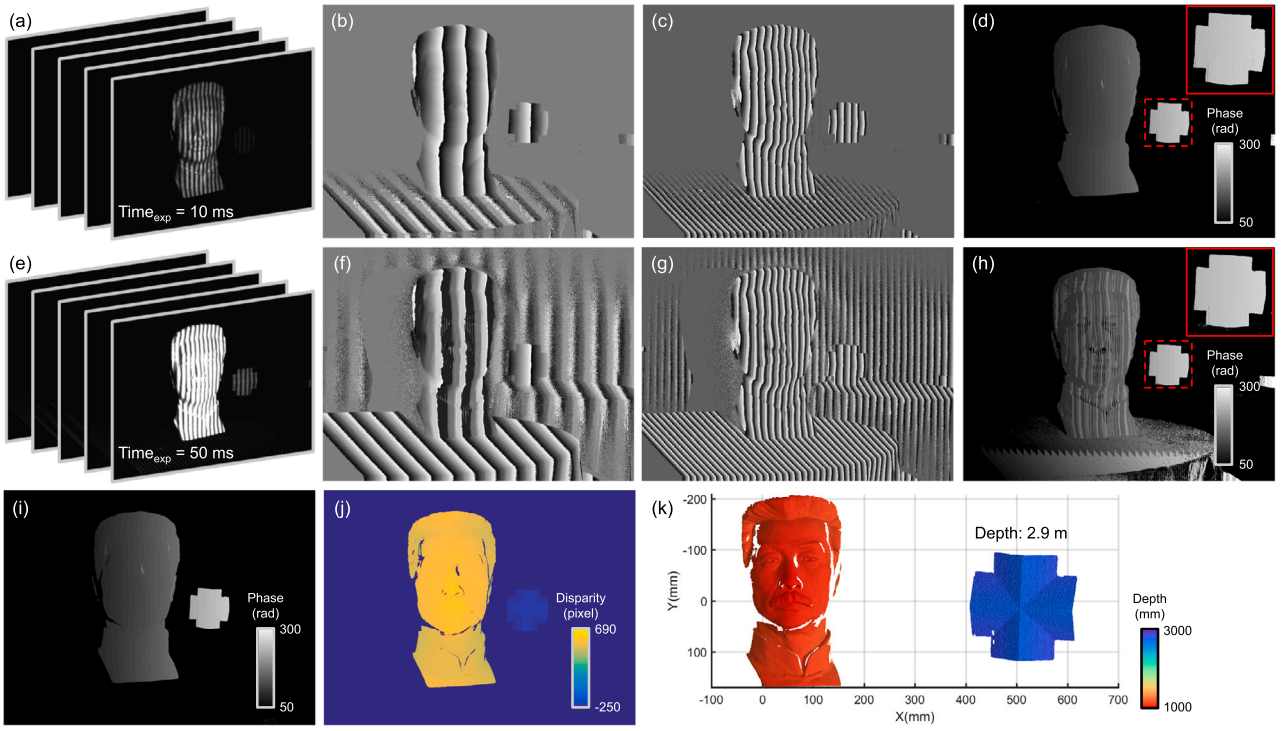

Fig. 4. Long-range 3D measurement results of complex targets for NT-TPU using the reference phases. (a)-(c) Bi-frequency (3+2) fringe images and the corresponding bi-frequency wrapped phases from the left camera with an exposure time of 10 ms. (d) The absolute phase map of (c). (e)-(g) Bi-frequency (3+2) fringe images and the corresponding bi-frequency wrapped phases from the left camera with an exposure time of 50 ms. (h) The absolute phase map of (g). (i) The mixed absolute phase using (d) and (h). (j) The disparity map output by stereo phase matching. (k) 3D reconstruction results of (j).

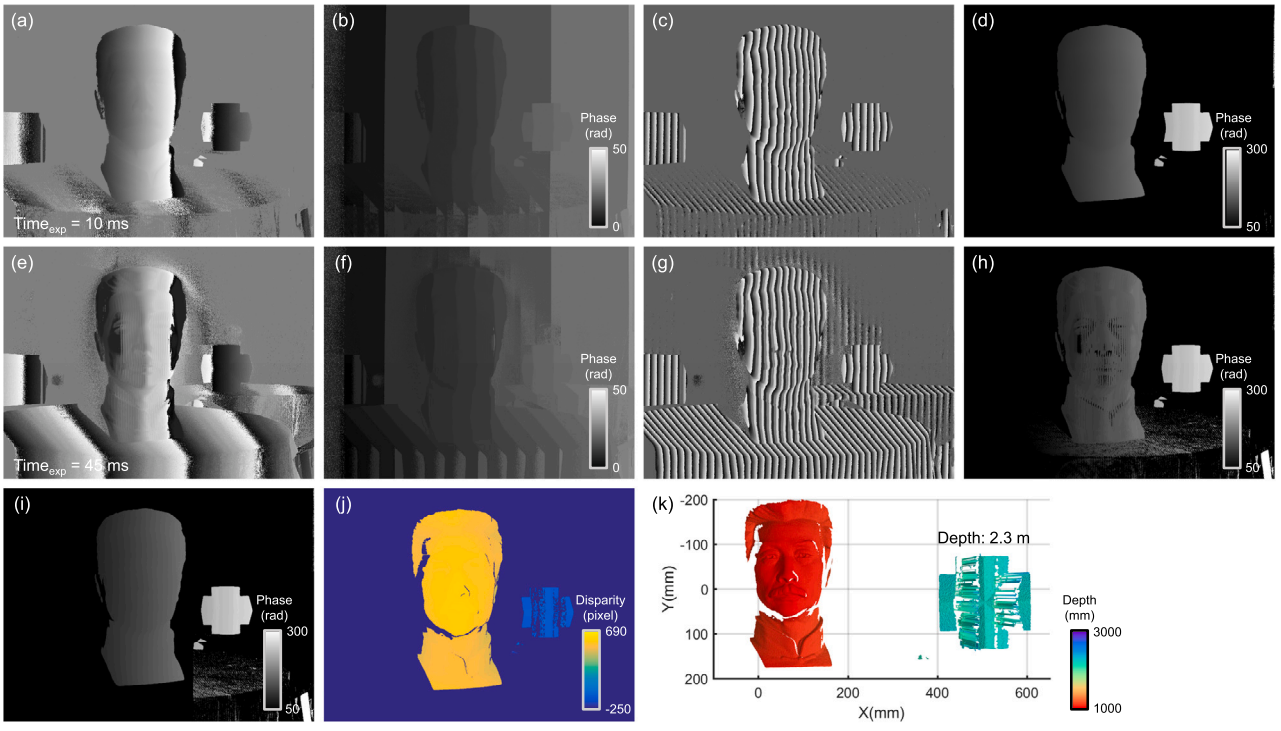

Fig. 5. Long-range 3D measurement results of complex targets for MF-TPU using the reference phases. (a)-(b) Low-frequency wrapped phase and the corresponding absolute phase obtained using the reference phases from the left camera with an exposure time of 10 ms. (c)-(d) High-frequency wrapped phase and the corresponding absolute phase using MF-TPU. (e)-(f) Low-frequency wrapped phase and the corresponding absolute phase obtained using the reference phases from the left camera with an exposure time of 45 ms. (g)-(h) High-frequency wrapped phase and the corresponding absolute phase using MF-TPU. (i) The mixed absolute phase using (d) and (h). (j) The disparity map output by stereo phase matching. (k) 3D reconstruction results of (j).

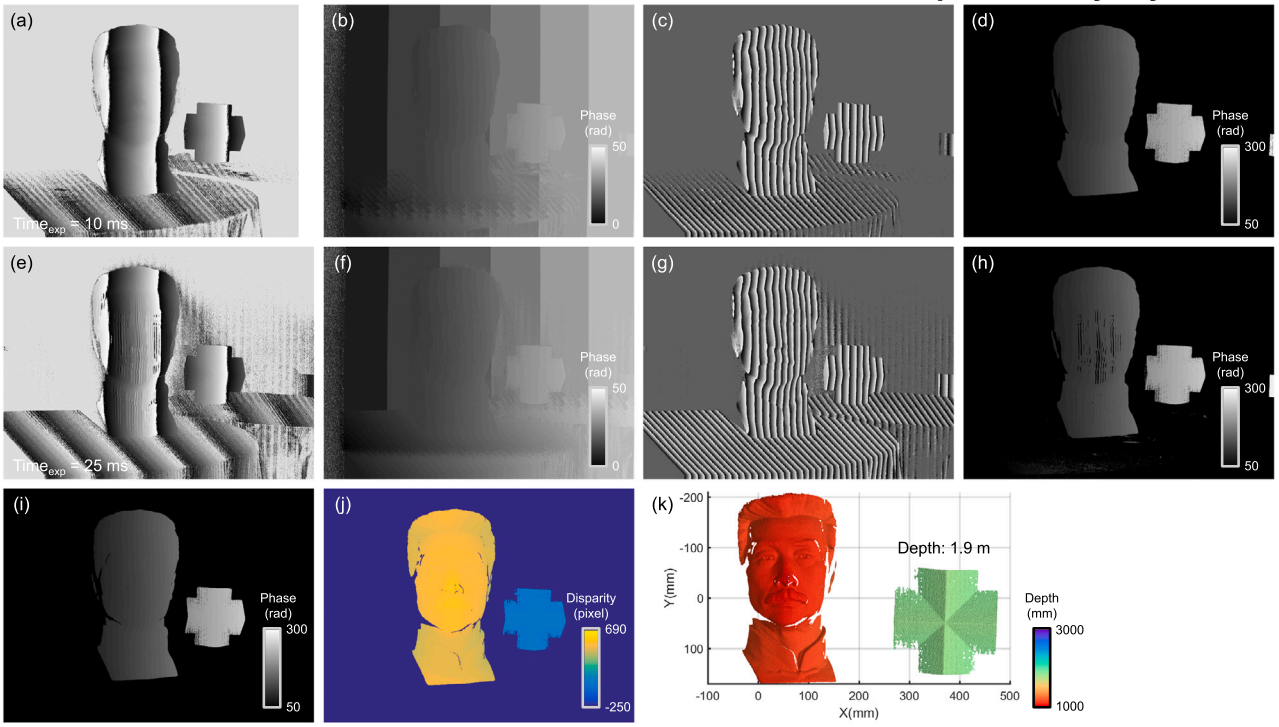

Fig. 6. Long-range 3D measurement results of complex targets for MW-TPU using the reference phases. (a)-(b) Synthetic wrapped phase and the corresponding absolute phase obtained using the reference phases from the left camera with an exposure time of 10 ms. (c)-(d) High-frequency wrapped phase and the corresponding absolute phase using MW-TPU. (e)-(f) Synthetic wrapped phase and the corresponding absolute phase obtained using the reference phases from the left camera with an exposure time of 25 ms. (g)-(h) High-frequency wrapped phase and the corresponding absolute phase using MW-TPU. (i) The mixed absolute phase using (d) and (h). (j) The disparity map output by stereo phase matching. (k) 3D reconstruction results of (j).

range is -250 pixels to 690 pixels, and the absolute disparity range is 941 pixels. Similarly, the measurement range of MW-TPU corresponds to a disparity range of 23 pixels to 690 pixels, and its absolute disparity range is 668 pixels. Therefore, the measured disparity range of NT-TPU is approximately 1.41 times that of MW-TPU, which is consistent with the experimental parameters in Table 1. Since the disparity changes less with increasing depth distance, the valid measuring range of NT-TPU is about twice that of MW-TPU in the depth plane. Finally, the experimental results similar to those of the simulation once again prove that the proposed method is capable of actualizing efficient and high-precision absolute 3D measurement within the large depth scope ranging from 1.0 m to 3.0 m, significantly enhancing the long-distance 3D imaging capability of existing methods using the reference phases.

On the other hand, we additionally provided a set of 3D measurement results of the rolled steels to test and verify the practicability of our 3D sensors in industrial scenarios. Long-distance, wide-field-of-view, and high-dynamic-range 3D imaging of large-scale and high-reflective industrial parts is crucial for automated feeding and blanking applications in intelligent manufacturing. Similarly, we extend the multi-exposure phase fusion strategy to adaptively synthesize the non-overexposed fringes in different areas as shown in Figs. 7(a)-(b), enabling high-completeness and high-precision 3D imaging of steels by capturing only 5+5 fringe images. These 3D reconstruction results demonstrate that our 3D sensors can be applied for high-quality and long-range 3D modeling of complex industrial structure parts as shown in Fig. 7(c).

3.2. Quantitative analysis of long-range 3D imaging accuracy

Thanks to the long detection capability of the MEMS projector equipped with an 8 W high-power laser, based on the developed 3D sensor (MEMS-3D), we conducted an experiment to quantitatively determine long-range 3D accuracy within the entire measurement volume. The test scene consists of a ceramic plane and a sphere pair with a diameter of 50.8 mm located at the depth scope ranging from 1.0 m to 3.0 m. Fig. 8 (a) shows the color-coded 3D reconstruction results at 1.1 m, and the precision analysis is carried out to obtain the corresponding 3D measurement errors for 50% valid areas of the measured targets by plane fitting and sphere fitting. Since the absolute phase of high-frequency fringe images with a wavelength of 19 pixels can be reliably recovered, the major measured errors of the plane and two spheres are less than 1 mm with the RMS of 0.1704 mm, 0.1339 mm, and 0.1459 mm as shown in Fig. 8 (b), respectively. As the measured distance increases in Fig. 8 (c), whether the planes or spheres are measured, our 3D sensor (MEMS-3D) can provide robust and high-precision 3D reconstruction results with a relative accuracy higher than 0.02% at 2.0 m and 0.04% at 3.0 m.

3.3. Fast 3D imaging of dynamic scenes

Different from the 3D sensor (MEMS-3D) dedicated to long-range 3D imaging, in Fig. 9(a), our miniaturized 3D sensor (MEMS-3D-Nano) is equipped with a high-performance ARM chip to process fringe images collected by high-speed CMOS cameras in real time, empowering fast 3D imaging applications on mobile terminals. Last, our miniaturized 3D sensor is applied to validate its fast and accurate 3D shape measurement capability by recording a dynamic scene in Fig. 9, including a David plaster and a Lu Xun model moving along the Z axis. In this experiment, the stereo camera, whose exposure time is set to 10 ms, can capture the optimal bi-frequency fringe images at 100 Hz for fast 3D imaging at 20 FPS. Figs. 9 (b)-(d) shows high-frequency fringe images and the corresponding color-coded 3D reconstruction results at different time points. During the whole dynamic measurement, two objects located in the center of the tested scene move along the Z axis to the extremity of the default 3D measurement range. The David plaster moves forward about 300 mm at a speed of 6 mm/s, while the Lu Xun model moves about 200

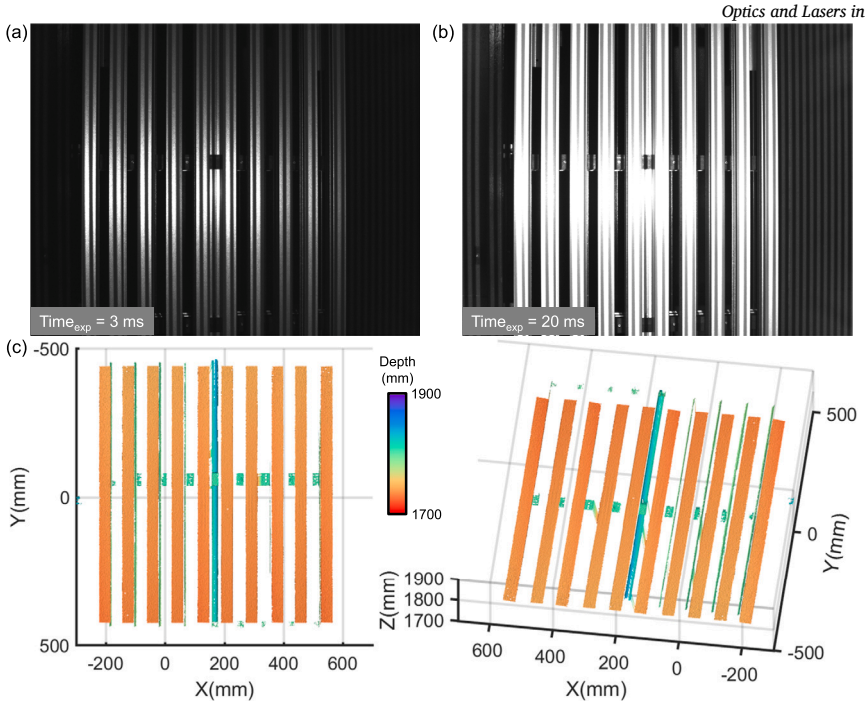

Fig. 7. Long-distance, wide-field-of-view, and high-dynamic-range 3D reconstruction of large-scale and high-reflective rolled steels. (a)-(b) High-frequency fringes with different exposure times of 3 ms and 20 ms. (c) 3D reconstruction results using the proposed method.

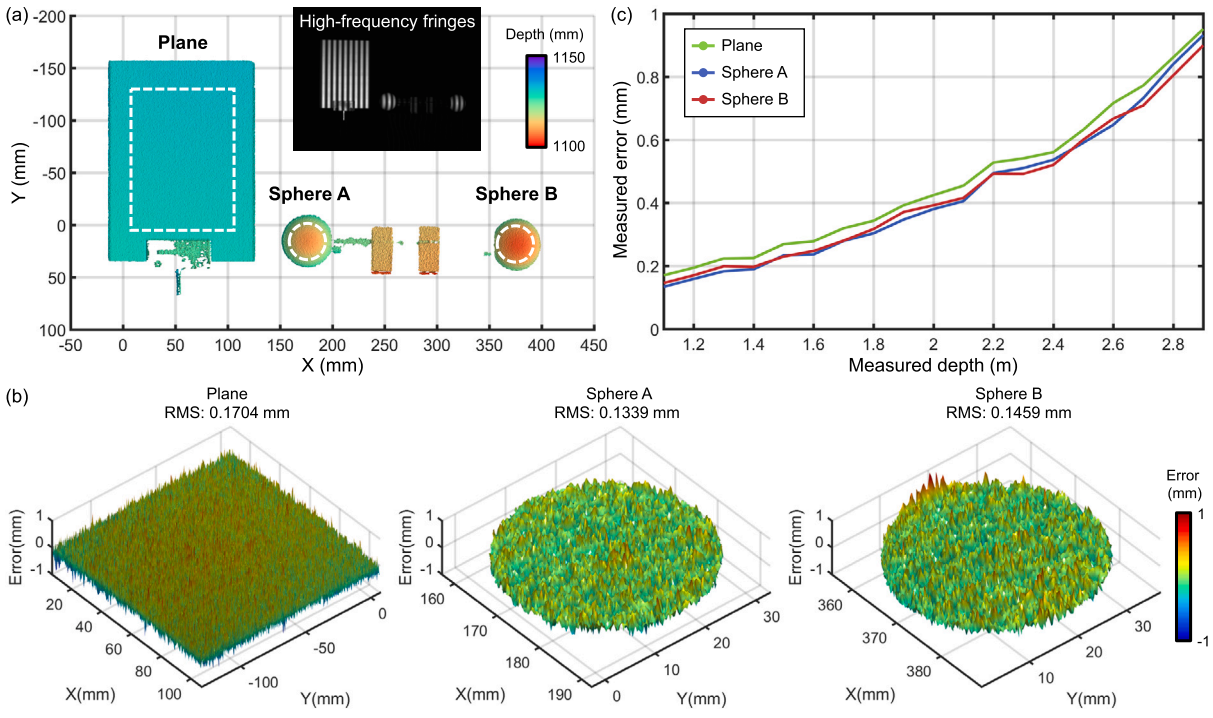

Fig. 8. Precision analysis for a ceramic plane and a sphere pair. (a)-(b) 3D reconstruction results using the proposed method, and the corresponding 3D measurement errors of the plane and spheres. (c) Precision analysis results of the plane and spheres at distances ranging from 1.0 m to 3.0 m.

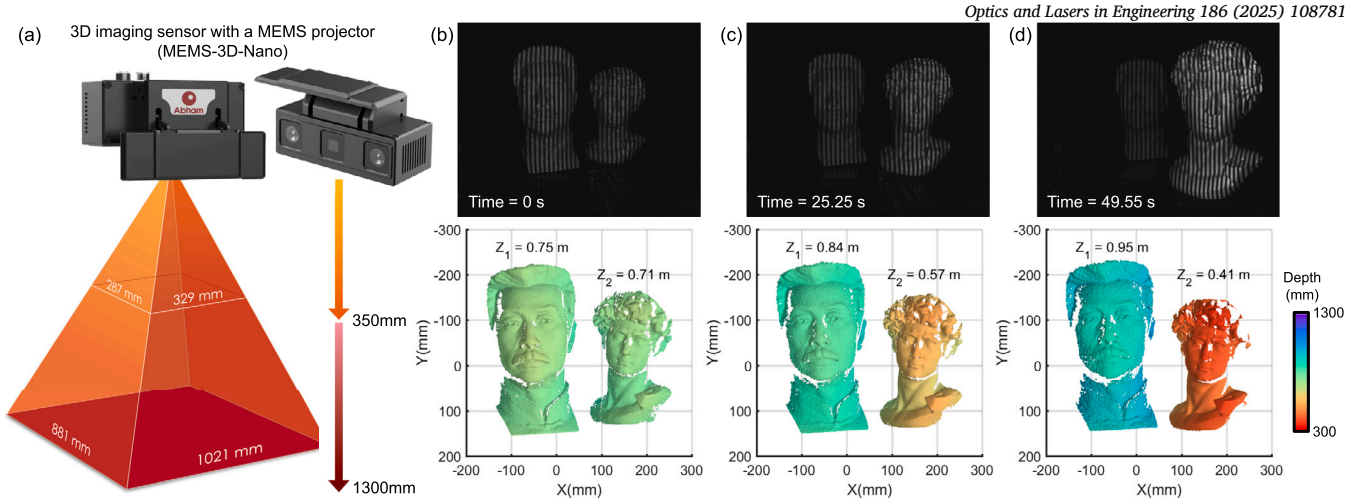

Fig. 9. Dynamic 3D measurement results including a David plaster and a Lu Xun model moving along the Z axis. (a) Photographs of the miniaturized 3D imaging sensor (MEMS-3D-Nano) with a MEMS projector. (b)-(d) High-frequency fringe images and the corresponding color-coded 3D reconstruction results at different time points.

mm in the reverse direction at 4 mm/s. The whole 3D reconstruction results can be found in Visualization 1. As the David plaster approaches the viewer, our sensor can output real-time 3D reconstruction results with high performance in the field of measurement resolution and accuracy. On the contrary, as the Lu Xun model gradually moves away from our 3D sensor, the contrast of the captured fringes decreases due to the fixed and short exposure time, resulting in the deteriorated quality of 3D reconstruction. The noise resistance of the proposed method is proved indirectly that it still achieves stable phase unwrapping to ensure high-integrity 3D measurement even in the presence of large phase errors. The reconstructed 3D point clouds at different time points show that our method can simultaneously and completely measure the 3D profiles of two isolated objects as they move away from each other.

4. Conclusions and discussion

In this work, we presented a fast and long-range 3D shape measurement method based on NT-TPU using the reference phases with a MEMS projector. The reference phases based on depth constraint are first introduced to adjust the phase ambiguities of number-theoretical approach from the traditional global scope to the local range, enabling absolute phase unwrapping of high-frequency fringes. Through modeling and analyzing the phase unwrapping performance of three classical TPU methods using the reference phases, an optimal bi-frequency fringe strategy is utilized to maximize the noise tolerance of phase unwrapping and increase the unambiguous 3D measurement range. Simulation results show that our method can achieve global and robust phase unwrapping over a larger depth range compared with MF-TPU and MW-TPU. Based on the proposed method, we developed two 3D sensors (named MEMS-3D and MEMS-3D-Nano) equipped with high-power and miniaturized MEMS projectors to actualize fast, wide-field-of-view, and high-precision 3D imaging for intelligent laser welding and 3D vision-guided robotic inspection. The long-distance measurement of two isolated large-sized objects verifies that our 3D sensor (MEMS-3D) can achieve high-efficiency 3D measurement in a large depth scope ranging from 1.0 m to 3.0 m using only 5 fringe patterns, while MF-TPU and MW-TPU using the reference phases cannot accurately reconstruct the target objects located at 2.3 m or 1.9 m, confirming the effectiveness of the proposed method once again. The precision analysis for the reconstructed point clouds of a planar target and a pair of standard spheres at different distances demonstrates that our method, whether measuring the plane or sphere, fulfills successfully robust and high-consistency 3D shape measurement with a relative accuracy higher than 0.02% at 2.0 m and 0.04% at 3.0 m. Finally, our miniaturized 3D sensor (MEMS-3D-Nano) is exploited to record a 3D dynamic scene including two isolated objects moving along the Z axis, demonstrating its applicability for real-time and accurate 3D measurement with high completeness.

We have analyzed and discussed the 3D imaging performance based on NT-TPU using the reference phases and a MEMS projector. In the future, we will improve the measurement accuracy and efficiency of 3D sensors by combining the three-frequency NT-TPU method with the reference phases. Further, the projection distance minimization algorithm [20] will be introduced to broaden the phase unambiguous range and enhance the noise tolerance, thus improving the reliability and measurement range of high-frequency phase unwrapping. On the other hand, how to hasten the computational efficiency of 3D imaging methods to run in real-time on general-purpose mobile platforms is our focus. Different from customized hardware platforms such as ASIC/FPGA, we will work on developing a high-performance 3D imaging framework based on the OpenCL environment to enable miniaturized and portable 3D sensing applications on ARM-based embedded chips. In terms of the hardware of FPP systems, it is worth considering the impact of the projector's defocus effect on long-distance 3D measurement. Given that the depth of fields corresponding to projected fringes of different frequencies is different [61], the phase fusion technique of different high-frequency fringes can be used to achieve long-range 3D measurement. In addition, the optical power and stability of the MEMS projector still need to be further enhanced.

CRediT authorship contribution statement

Wei Yin: Writing – review & editing, Writing – original draft, Visualization, Methodology, Funding acquisition. **Long Yin:** Writing – original draft, Validation, Methodology. **Xu Yang:** Validation, Methodology. **Shijie Feng:** Writing – review & editing, Writing – original draft, Supervision. **Xiaolei Zhang:** Writing – review & editing, Writing – original draft, Funding acquisition. **Huai Wang:** Visualization, Validation. **Qian Chen:** Writing – review & editing, Writing – original draft, Supervision, Funding acquisition. **Chao Zuo:** Writing – review & editing, Writing – original draft, Visualization, Validation, Supervision, Methodology, Funding acquisition.

Declaration of competing interest

The authors declare that they have no known competing financial interests or personal relationships that could have appeared to influence the work reported in this paper.

Acknowledgements

This work was supported by National Key Research and Development Program of China (2022YFB2804603, 2022YFB2804604), National Natural Science Foundation of China (62205147, 62075096, U21B2033), China Postdoctoral Science Foundation (2023T160318, 2022M711630), Jiangsu Funding Program for Excellent Postdoctoral Talent (2022ZB254), The Leading Technology of Jiangsu Basic Research Plan (BK20192003), The “333 Engineering” Research Project of Jiangsu Province (BRA2016407), The Jiangsu Provincial “One belt and one road” innovation cooperation project (BZ2020007), Open Research Fund of Jiangsu Key Laboratory of Spectral Imaging & Intelligent Sense (JSGP202105), Fundamental Research Funds for the Central Universities (30922010405, 30921011208, 30920032101, 30919011222), and National Major Scientific Instrument Development Project (62227818).

Data availability

Data will be made available on request.

References

[1] Gåsvik KJ. Optical metrology. John Wiley & Sons; 2003.
[2] Zuo C, Qian J, Feng S, Yin W, Li Y, Fan P, et al. Deep learning in optical metrology: a review. Light: Sci Appl 2022;11:1–54.
[3] Sun J, Zheng N-N, Shum H-Y. Stereo matching using belief propagation. IEEE Trans Pattern Anal Mach Intell 2003;25:787–800.
[4] Hirschmuller H. Stereo processing by semiglobal matching and mutual information. IEEE Trans Pattern Anal Mach Intell 2007;30:328–41.
[5] Mei X, Sun X, Zhou M, Jiao S, Wang H, Zhang X. On building an accurate stereo matching system on graphics hardware. In: 2011 IEEE international conference on computer vision workshops. IEEE; 2011. p. 467–74.
[6] Zhang L, Zhan H, Liu X, Cao H, Xing F, You Z. A planar compound eye based microsystem for high precision 3d perception. PhotoniX 2024;5:1–14.
[7] Fan Z-B, Cheng Y-F, Chen Z-M, Liu X, Lu W-L, Li S-H, et al. Integral imaging near-eye 3d display using a nanoimprint metalens array. eLight 2024;4:3.
[8] Ganapathi V, Plagemann C, Koller D, Thrun S. Real time motion capture using a single time-of-flight camera. In: 2010 IEEE computer society conference on computer vision and pattern recognition. IEEE; 2010. p. 755–62.
[9] Kolb A, Barth E, Koch R, Larsen R. Time-of-flight cameras in computer graphics. In: Computer graphics forum. Wiley Online Library; 2010. p. 141–59.
[10] Hansard M, Lee S, Choi O, Horaud RP. Time-of-flight cameras: principles, methods and applications. Springer Science & Business Media; 2012.
[11] Park J, Gao L. Cascaded compressed-sensing single-pixel camera for high-dimensional optical imaging. PhotoniX 2024;5:37.
[12] Van Gestel N, Cuypers S, Bleys P, Kruth J-P. A performance evaluation test for laser line scanners on cmms. Opt Lasers Eng 2009;47:336–42.
[13] Gorthi SS, Rastogi P. Fringe projection techniques: whither we are? Opt Lasers Eng 2010;48:133–40.
[14] Feng S, Zhang L, Zuo C, Tao T, Chen Q, Gu G. High dynamic range 3d measurements with fringe projection profilometry: a review. Meas Sci Technol 2018;29:122001.
[15] Zhang S. Absolute phase retrieval methods for digital fringe projection profilometry: a review. Opt Lasers Eng 2018;107:28–37.
[16] Yin W, Feng S, Tao T, Huang L, Zhang S, Chen Q, et al. Calibration method for panoramic 3d shape measurement with plane mirrors. Opt Express 2019;27:36538–50.
[17] Takeda M, Mutoh K. Fourier transform profilometry for the automatic measurement of 3-d object shapes. Appl Opt 1983;22:3977–82.
[18] Su X, Chen W. Fourier transform profilometry:: a review. Opt Lasers Eng 2001;35:263–84.
[19] Mao X, Chen W, Su X. Improved Fourier-transform profilometry. Appl Opt 2007;46:664–8.
[20] Zuo C, Tao T, Feng S, Huang L, Asundi A, Chen Q. Micro Fourier transform profilometry (μ ftp): 3d shape measurement at 10,000 frames per second. Opt Lasers Eng 2018;102:70–91.
[21] Zuo C, Feng S, Huang L, Tao T, Yin W, Chen Q. Phase shifting algorithms for fringe projection profilometry: a review. Opt Lasers Eng 2018;109:23–59.
[22] Feng S, Chen Q, Gu G, Tao T, Zhang L, Hu Y, et al. Fringe pattern analysis using deep learning. Adv Photon 2019;1:025001.
[23] Yin W, Che Y, Li X, Li M, Hu Y, Feng S, et al. Physics-informed deep learning for fringe pattern analysis. Optoelectron Adv 2024;7(1):230034.
[24] Herráez MA, Burton DR, Lalor MJ, Gdeisat MA. Fast two-dimensional phase-unwrapping algorithm based on sorting by reliability following a noncontinuous path. Appl Opt 2002;41:7437–44.
[25] Su X, Chen W. Reliability-guided phase unwrapping algorithm: a review. Opt Lasers Eng 2004;42:245–61.
[26] Su X, Zhang Q. Dynamic 3-d shape measurement method: a review. Opt Lasers Eng 2010;48:191–204.
[27] Zhao M, Huang L, Zhang Q, Su X, Asundi A, Kemao Q. Quality-guided phase unwrapping technique: comparison of quality maps and guiding strategies. Appl Opt 2011;50:6214–24.
[28] Wang Y, Zhang S. Novel phase-coding method for absolute phase retrieval. Opt Lett 2012;37:2067–9.
[29] Zuo C, Huang L, Zhang M, Chen Q, Asundi A. Temporal phase unwrapping algorithms for fringe projection profilometry: a comparative review. Opt Lasers Eng 2016;85:84–103.
[30] Yin W, Zuo C, Feng S, Tao T, Hu Y, Huang L, et al. High-speed three-dimensional shape measurement using geometry-constraint-based number-theoretical phase unwrapping. Opt Lasers Eng 2019;115:21–31.
[31] Yin W, Chen Q, Feng S, Tao T, Huang L, Trusiak M, et al. Temporal phase unwrapping using deep learning. Sci Rep 2019;9:20175.
[32] Wu Z, Zuo C, Guo W, Tao T, Zhang Q. High-speed three-dimensional shape measurement based on cyclic complementary gray-code light. Opt Express 2019;27:1283–97.
[33] Wu Z, Guo W, Zhang Q. Two-frequency phase-shifting method vs. gray-coded-based method in dynamic fringe projection profilometry: a comparative review. Opt Lasers Eng 2022;153:106995.
[34] Weise T, Leibe B, Van Gool L. Fast 3d scanning with automatic motion compensation. In: 2007 IEEE conference on computer vision and pattern recognition. IEEE; 2007. p. 1–8.
[35] Garcia RR, Zakhor A. Consistent stereo-assisted absolute phase unwrapping methods for structured light systems. IEEE J Sel Top Signal Process 2012;6:411–24.
[36] Li Z, Zhong K, Li YF, Zhou X, Shi Y. Multiview phase shifting: a full-resolution and high-speed 3d measurement framework for arbitrary shape dynamic objects. Opt Lett 2013;38:1389–91.
[37] Zhong K, Li Z, Shi Y, Wang C, Lei Y. Fast phase measurement profilometry for arbitrary shape objects without phase unwrapping. Opt Lasers Eng 2013;51:1213–22.
[38] Song K, Hu S, Wen X, Yan Y. Fast 3d shape measurement using Fourier transform profilometry without phase unwrapping. Opt Lasers Eng 2016;84:74–81.
[39] Tao T, Chen Q, Da J, Feng S, Hu Y, Zuo C. Real-time 3-d shape measurement with composite phase-shifting fringes and multi-view system. Opt Express 2016;24:20253–69.
[40] Tao T, Chen Q, Feng S, Hu Y, Zhang M, Zuo C. High-precision real-time 3d shape measurement based on a quad-camera system. J Opt 2017;20:014009.
[41] Yin W, Feng S, Tao T, Huang L, Trusiak M, Chen Q, et al. High-speed 3d shape measurement using the optimized composite fringe patterns and stereo-assisted structured light system. Opt Express 2019;27:2411–31.
[42] Huntley JM, Saldner H. Temporal phase-unwrapping algorithm for automated interferogram analysis. Appl Opt 1993;32:3047–52.
[43] Zhao H, Chen W, Tan Y. Phase-unwrapping algorithm for the measurement of three-dimensional object shapes. Appl Opt 1994;33:4497–500.
[44] Towers CE, Towers DP, Jones JD. Optimum frequency selection in multifrequency interferometry. Opt Lett 2003;28:887–9.
[45] Towers C, Towers D, Jones J. Absolute fringe order calculation using optimised multi-frequency selection in full-field profilometry. Opt Lasers Eng 2005;43:788–800.
[46] Zhong J, Wang M. Phase unwrapping by lookup table method: application to phase map with singular points. Opt Eng 1999;38:2075–80.
[47] Zhong J, Zhang Y. Absolute phase-measurement technique based on number theory in multifrequency grating projection profilometry. Appl Opt 2001;40:492–500.
[48] Zuo C, Chen Q, Gu G, Feng S, Feng F, Li R, et al. High-speed three-dimensional shape measurement for dynamic scenes using bi-frequency tripolar pulse-width-modulation fringe projection. Opt Lasers Eng 2013;51:953–60.
[49] An Y, Hyun J-S, Zhang S. Pixel-wise absolute phase unwrapping using geometric constraints of structured light system. Opt Express 2016;24:18445–59.
[50] Hyun J-S, Zhang S. Superfast 3d absolute shape measurement using five binary patterns. Opt Lasers Eng 2017;90:217–24.
[51] Hyun J-S, Zhang S. Enhanced two-frequency phase-shifting method. Appl Opt 2016;55:4395–401.
[52] Duan M, Jin Y, Chen H, Kan Y, Zhu C, Chen E. Dynamic 3-d shape measurement in an unlimited depth range based on adaptive pixel-by-pixel phase unwrapping. Opt Express 2020;28:14319–32.
[53] Guan Y, Yin Y, Li A, Liu X, Peng X. Dynamic 3d imaging based on acousto-optic heterodyne fringe interferometry. Opt Lett 2014;39:3678–81.
[54] Chen W, Feng S, Yin W, Li Y, Qian J, Chen Q, et al. Deep-learning-enabled temporally super-resolved multiplexed fringe projection profilometry: high-speed khz 3d imaging with low-speed camera. PhotoniX 2024;5:25.
[55] Zhang S, Huang PS. Novel method for structured light system calibration. Opt Eng 2006;45:083601.
[56] Li Z, Shi Y, Wang C, Wang Y. Accurate calibration method for a structured light system. Opt Eng 2008;47:053604.
[57] Zhang Z, Ma H, Zhang S, Guo T, Towers CE, Towers DP. Simple calibration of a phase-based 3d imaging system based on uneven fringe projection. Opt Lett 2011;36:627–9.
[58] Wan T, Liu Y, Zhou Y, Liu X. Large-scale calibration method for mems-based projector 3d reconstruction. Opt Express 2023;31:5893–909.
[59] Qu J, Gao H, Zhang R, Cao Y, Zhou W, Xie H. High-flexibility and high-accuracy phase delay calibration method for mems-based fringe projection systems. Opt Express 2023;31:1049–66.

[60] Ding Y, Xi J, Yu Y, Cheng W, Wang S, Chicharo JF. Frequency selection in absolute phase maps recovery with two frequency projection fringes. Opt Express 2012;20:13238–51.

[61] Rao G, Song L, Zhang S, Yang X, Chen K, Xu J. Depth-driven variable-frequency sinusoidal fringe pattern for accuracy improvement in fringe projection profilometry. Opt Express 2018;26:19986–20008.